Materials & Design 233 (2023) 112294

Contents lists available at ScienceDirect

Materials & Design

journal homepage: www.elsevier.com/locate/matdes

Investigation of the strain rate sensitivity of CoCrFeMnNiTi$_x$ (x = 0, 0.3) high-entropy alloys using the shear punch test

S. González [a,*], A.K. Sfikas [a], S. Kamnis [b], S.E. John [c], N.C. Barnard [c], C. Gammer [d], J. Eckert [d,g], C.G. Garay-Reyes [e], R. Martínez-Sánchez [e], S.W. Naung [a], M. Rahmati [a], T. Keil [f], K. Durst [f], R.J. Lancaster [c]

[a] Faculty of Engineering and Environment, Northumbria University, Newcastle upon Tyne NE1 8ST, United Kingdom
[b] Castolin Eutectic-Monitor Coatings Ltd, Newcastle upon Tyne NE29 8SE, United Kingdom
[c] Institute of Structural Materials, Faculty of Science & Engineering, Bay Campus, Swansea University, Swansea SA1 8EN, United Kingdom
[d] Erich Schmid Institute of Materials Science, Austrian Academy of Sciences, Jahnstraße 12, 8700 Leoben, Austria
[e] Centro de Investigación en Materiales Avanzados (CIMAV), Laboratorio Nacional de Nanotecnología, Miguel de Cervantes 120, 31136 Chihuahua, Chih., Mexico
[f] Materials Science, Physical Metallurgy, Technical University of Darmstadt, Darmstadt D-64287, Germany
[g] Department of Materials Science, Montanuniversit¨at Leoben, Jahnstraße 12, 8700 Leoben, Austria

ARTICLE INFO

Keywords:
Shear punch testing
High entropy alloy
Finite element simulation

ABSTRACT

High entropy alloys (HEAs) are a novel class of metallic materials that exhibit a unique blend of properties due to their chemical composition and atomic arrangement. This research aims to investigate the strain rate sensitivity (SRS) of two HEA CoCrFeMnNiTi$_x$ (x = 0, 0.3) alloy compositions through the use of shear punch testing. This method has been proven to provide reliable results for both HEA materials, including the CoCrFeMnNiTi0.3 HEA composition which was found to be inherently brittle and contained both σ-phase and Laves phase compounds with a hardness close to 14 GPa and a soft FCC phase. Among all the testing temperatures (room temperature to 400 °C) and deflection rates (0.2, 2 and 10 mm.min^{-1}) used, only the CoCrFeMnNi HEA alloy was found to exhibit SRS at room temperature (m = 0.0333), while for the other HEA alloy variant and testing conditions, the SRS was found to be zero. From empirical correlations and finite element analysis (FEA), the calculated value for m ranged from 0.0333 to 0.0359, thus evidencing that the FEA simulations provide an accurate and suitable means of capturing the deformation behaviour of such alloys when subjected to shearing.

1. Introduction

High entropy alloys (HEAs) are a class of metallic alloys with similar concentrations of 5 or more elements [1,2]. They exhibit the four core effects, which include sluggish diffusion, high-entropy, lattice distortion and cocktail effect [3]. The interest of HEAs stems from their superior properties including high corrosion resistance, wear resistance, strength and thermal stability [4]. Among them, the CoCrFeMnNi alloy (i.e., Cantor alloy) is particularly promising because of the favourable fracture toughness and ductility properties it offers, yet it exhibits relatively low strength. The strength can be enhanced with addition of dopants such as Ti since it promotes the formation of precipitates that can prevent grain growth [5]. This element also decreases the stability of the FCC phase due to the larger atomic radius of Ti compared to the size of the other elements and also increases the likelihood of σ phase formation [6]. The addition of Ti in bulk CoCrFeMnNi HEAs has been reported to increase the volume fraction of strengthening precipitates [6] and therefore enhancing the mechanical properties [7,8]. However, the extent of such improvement is highly dependent on its concentration. Low additions of Ti ($Ti_{0.1}$ and $Ti_{0.3}$) in CoCrFeMnNi results in the formation of Ti oxide particles embedded in a FCC solid solution matrix, but even minor additions are known to have a positive effect on the mechanical properties by solid solution strengthening [8]. These authors observed an improvement in tensile strength without losing ductility by adding 0.3 at. % Ti. This alloy can therefore have industrial interest as load-bearing materials. When the concentration of Ti is increased ($Ti_{0.4}$), secondary Cr and Ti rich sigma (σ) phase is formed, which is an inherently brittle phase. For the CoCrFeNiTi 0.5 alloy, Shahmir et al. [8] reported the formation of (Ti, Co)-rich Laves phase and R + σ mixed phases, inducing a brittle behaviour in the alloy. For this reason, in order

* Corresponding author.
E-mail address: sergio.sanchez@northumbria.ac.uk (S. González).

https://doi.org/10.1016/j.matdes.2023.112294
Received 28 May 2023; Received in revised form 28 August 2023; Accepted 29 August 2023
Available online 1 September 2023

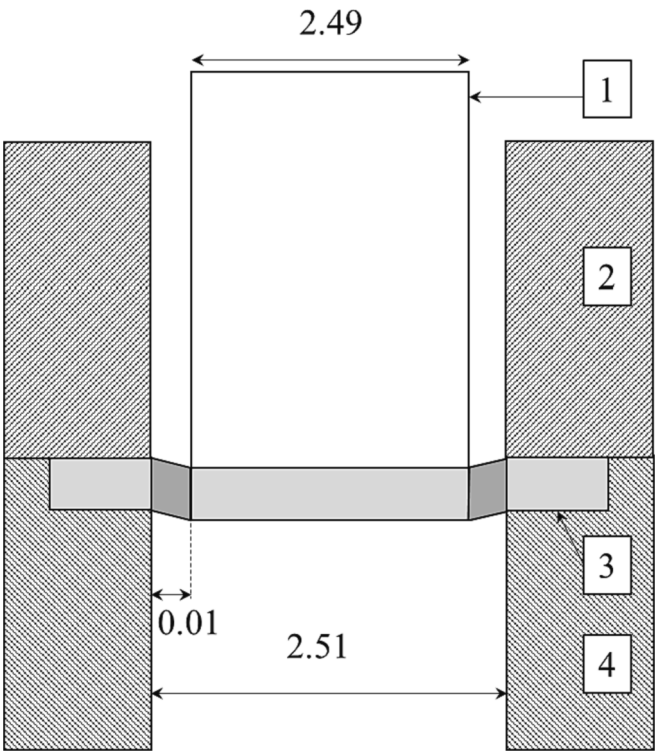

Fig. 1. Schematic representation of the shear punch test assembly.

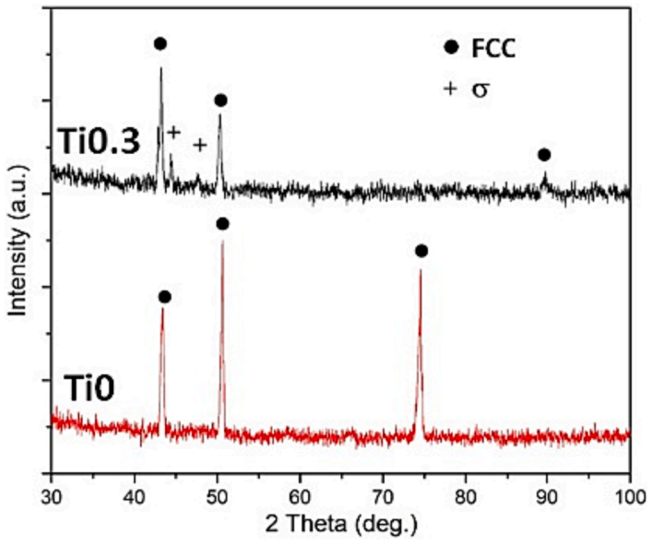

Fig. 2. XRD patterns of the as-cast CoCrFeMnNi (Ti0) and CoCrFeMnNi$Ti_{0.3}$ (Ti0.3) alloys.

to prevent alloy embrittlement, higher concentrations of Ti additions are not recommended. As such, for the optimal compromise of strength and ductility, the CoCrFe(Mn)NiTi$_{0.3}$ composition is currently one of the most favoured blends of chemical elements for HEAs [8,9].

One of the main drawbacks when assessing the mechanical properties of HEAs is their relative high cost, and for this reason it is of interest to reduce the usage of material for testing as much as possible. Among all the methods to assess the mechanical performance of materials, small punch (SP) testing profits from the economic benefit of using a small sample size [10]. In the SP test, a miniature disc is subjected to a compressive force transferred through a hemispherical punch indenter, promoting a behaviour akin to tensile deformation. However, this punch indenter geometry may not yield sufficient results for materials with reduced ductility or those containing a lower amount of slip systems, like that seen in a Ti based alloy containing a hexagonally close packed (HCP) lattice [11]. An alternative testing means to prevent this issue is the shear punch (ShP) test, which has a similar experimental arrangement but consists of a flat ended punch which in turn promotes a compressive force in the middle of the specimen, thus inducing a shearing mode of deformation around the edges. This enables a more uniform stress and therefore is more suitable for relatively brittle materials. Moreover, in comparison to the results generated from the SP test, the properties predicted from the ShP test across a range of metallic systems have been found to offer a stronger fit to more recognised uniaxial properties [11].

The mechanical behaviour of relatively few materials have been assessed so far from ShP tests, mostly commercial alloys such as magnesium, brass, steel [12,13] aluminium and some aluminium alloys [14]. Also, some non-commercial alloys including more brittle alloys, such as metallic glasses and their composites have been studied from ShP tests [15,16], but very few HEAs such as $Co_{20}Cr_{20}Fe_{20}Ni_{20}Mn_{15}Cu_5$ at. % HEA have been assessed in this way [17]. However, in all these cases ShP tests were used to assess the ultimate shear stress while this work aims to obtain the strain rate sensitivity. As far as the authors are concerned, the only punch testing research performed so far to analyse the strain rate sensitivity of a HEA (i.e., $m = 0.1387$ experimentally and $m = 0.1313$ from simulations) was reported by González et al. [18] but was solely performed at room temperature (RT). Here, the research presented in this paper will focus on the application of the ShP test both at RT and at 400 °C on the HEA compositions of CoCrFeMnNi and CoCrFeMnNi$Ti_{0.3}$. Due to the increasing technological importance of HEAs, especially of those exhibiting high strength and ductility, it is of interest to study their strain rate sensitivity to quantify their tendency to creep (when they do not creep they have a near-zero strain rate sensitivity.). This research could therefore be relevant for industrial applications, for example as fail-safe mechanisms or as energy absorbing materials.

2. Experimental methods

2.1. Materials and Microscopy

Alloy ingots of nominal composition CoCrFeMnNi and CoCrFeMnNi$Ti_{0.3}$ (coded as Ti0 and Ti0.3 in this work) were prepared from elements with purity higher than 99.9 at.%. The master alloys were remelted (heated to a red heat) multiple times in a Ti-gettered high purity argon atmosphere to attain chemical homogeneity using suction casting arc melting. Cylindrical rods of 8 mm diameter were obtained from the master alloy by copper mold casting in an inert gas atmosphere and a cooling system set at 20 °C. The structure of the as-cast samples was studied by a SmartLab Rigaku XRD diffractometer with monochromated Cu Kα radiation (25 deg – 90 deg 2θ range). The microstructure was investigated with a Mira 3 Scanning Electron Microscope (SEM) TESCAN equipped with an electron backscatter diffraction (EBSD) detector as well as an energy-dispersive X-ray (EDX) detector.

2.2. Mechanical testing

2.2.1. Shear punch testing

The disc specimens of CoCrFeMnNi and CoCrFeMnNi$Ti_{0.3}$ were obtained by sectioning the 8 mm cylinders of the alloy into slices of approximately 800 μm in thickness. Using a custom designed specimen holder, the discs were progressively ground and polished on both faces with finer silicon carbide abrasive papers until the required specimen thickness of 500 μm ± 5 μm with a 1200 grit finish was achieved. These procedures are in direct accordance with the recommendations defined in the EN and ASTM standards [19,20]. Shear punch (ShP) tests were performed on a bespoke jig assembly, as previously reported in [21].

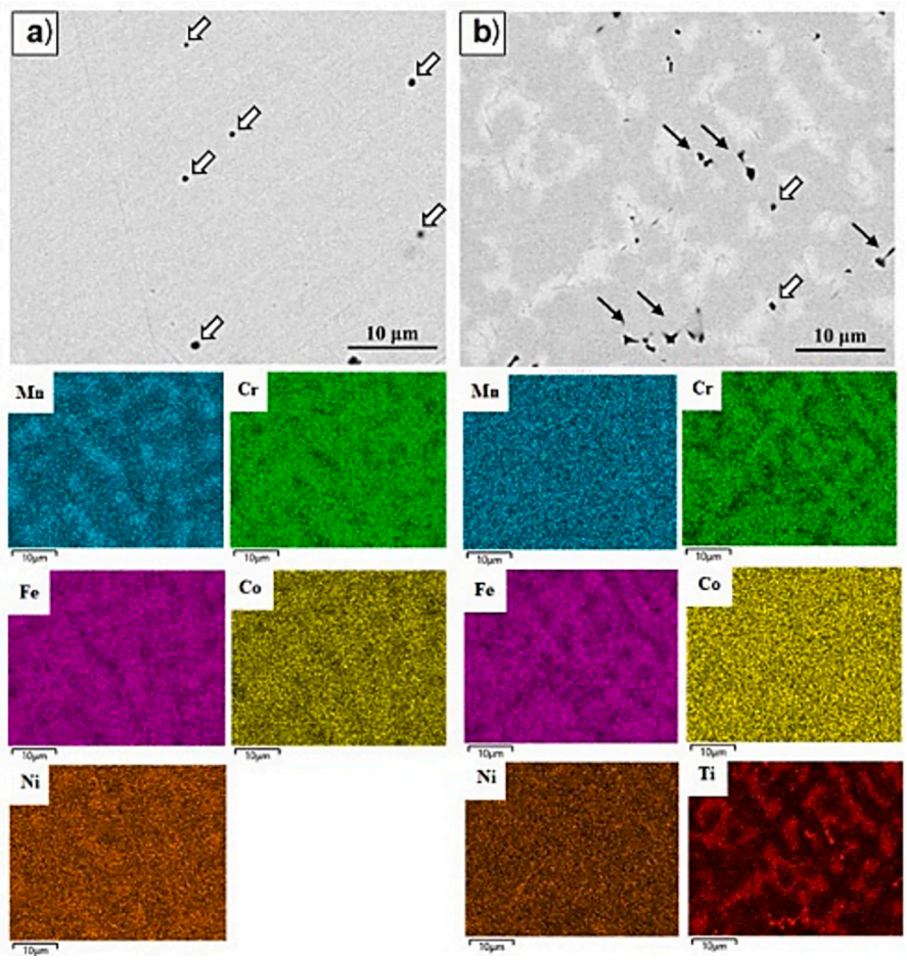

Fig. 3. Backscattered Electron SEM images for a) CoCrFeMnNi (Ti0), and b) $CoCrFeMnNiTi_{0.3}$ (Ti0.3) and corresponding compositional X-ray mappings for Mn, Cr, Fe, Co, Ni and Ti.

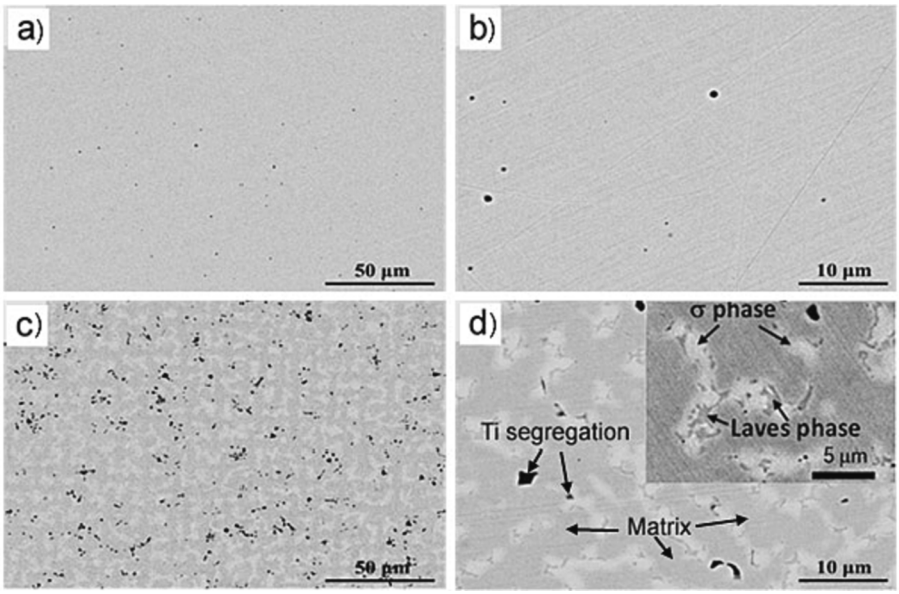

Fig. 4. SEM images at two different magnifications for (a and b) CoCrFeMnNi (Ti0), (c and d) $CoCrFeMnNiTi_{0.3}$ (Ti0.3) HEA alloys.

Similarly to SP testing, the jig assembly locates into a 5kN electric screw test machine and comprises of an upper (2) and lower die (4) set to clamp the disc specimen (3) (as depicted in Fig. 1). The upper die typically has a ϕ4 mm receiving hole, whilst the lower die has a 0.2 mm chamfer above the receiving hole, which has a diameter of 2.51 mm, as shown in Fig. 1.

Table 1
Volume fraction of the crystalline phases for the Ti0.3 HEA.

Phases	$CoCrFeMnNiTi_{0.3}$ (vol. %)
Grey dendrites	63
Laves phase	2
σ phase	27
Ti-rich particles + porosity	8

When the test frame cross-head is in contact with the flat surface of the push collar, a compressive movement applies a force to the disc specimen through a flat-ended punch head, which has a diameter of 2.49 mm. As previously shown by Hankin et al. [22], the true multiaxial, non-uniform stress state in the annular shear zone, is a relatively uniform shear in conjunction with a small compressive stress. Plus, since there is a widening of the stress field with decreasing stress amplitude outside of the annular region defined by the punch clearance, the combined effect of these multiaxial, non-uniform stresses relative to a pure shear stress state can be accounted for through modifications in the correlation constants connecting the ShP test stresses to uniaxial tensile stresses [22]. As such, Eq. (1) can be adopted as an appropriate definition of shear stress (τ) for the ShP tests, which is calculated through the following equation:

$$\tau = \frac{F}{2\pi r_{avg} t} \tag{1}$$

Where F is the punch load and r_{avg} is the average of the radius of the punch head and the radius of the receiving hole ($r_{avg} = r_{punch} + r_{die} / 2$). The resulting deformation behaviour has many similarities to a σ-ε curve from a uniaxial tensile test, such as an initial linear elastic region, a yield point, a period of plastic deformation until reaching an ultimate load followed by failure.

Residual deflection measurements are recorded via an adapted transducer rod which connects the center of the underneath surface of the specimen to a linear variable deflection transducer (LVDT), providing deflection measurements directly from the specimen, to accompany the deflection behaviour recorded from the crosshead movement. All tests were performed under deflection control to replicate tensile deformation, where a range of crosshead deflection rates were adopted, varying from 0.2 to 10 mm•min^{-1}. Deflection and force values were recorded every 0.1 s during testing. Experiments were performed at least twice at ambient room temperature in a controlled laboratory environment (21 °C), and at 400 °C. Elevated temperature testing was conducted by encasing the jig assembly within a three-zone radiant furnace. Two N-type thermocouples were used to monitor the disc temperatures to ensure they fell within ± 0.25 % of the desired test temperature in degrees Celsius, °C (for a 400 °C test, the tolerance is ± 1 °C).

2.2.2. Nanoindentation

The indentation modulus and hardness maps of the CoCrFeMnNi and $CoCrFeMnNiTi_{0.3}$ HEAs were assessed using the NanoBlitz 3D method of the iNano nanoindentation system (KLA instruments) using a Berkovich diamond tip. The indentation mapping was performed on a representative section from the central radius of the samples with a size of 70 × 70 μm^2. The hardness and modulus data were evaluated using the Oliver and Pharr approach [23] at a maximum load of 15 mN. Due to the different indentation depths, the spacing between each indent was set to 4 μm for the CoCrFeMnNi alloy and to 2 μm for the $CoCrFeMnNiTi_{0.3}$ alloy. The testing was thus performed using a grid of 26 × 26 indentations producing a total of 361 (CoCrFeMnNi) or 1296 ($CoCrFeMnNiTi_{0.3}$) indents. The strain rate sensitivity was further investigated using nanoindentation strain rate jump (SRJ) testing. The applied strain rate was varied between 0.05 s^{-1}, 0.005 s^{-1} and 0.001 s^{-1} for every 500

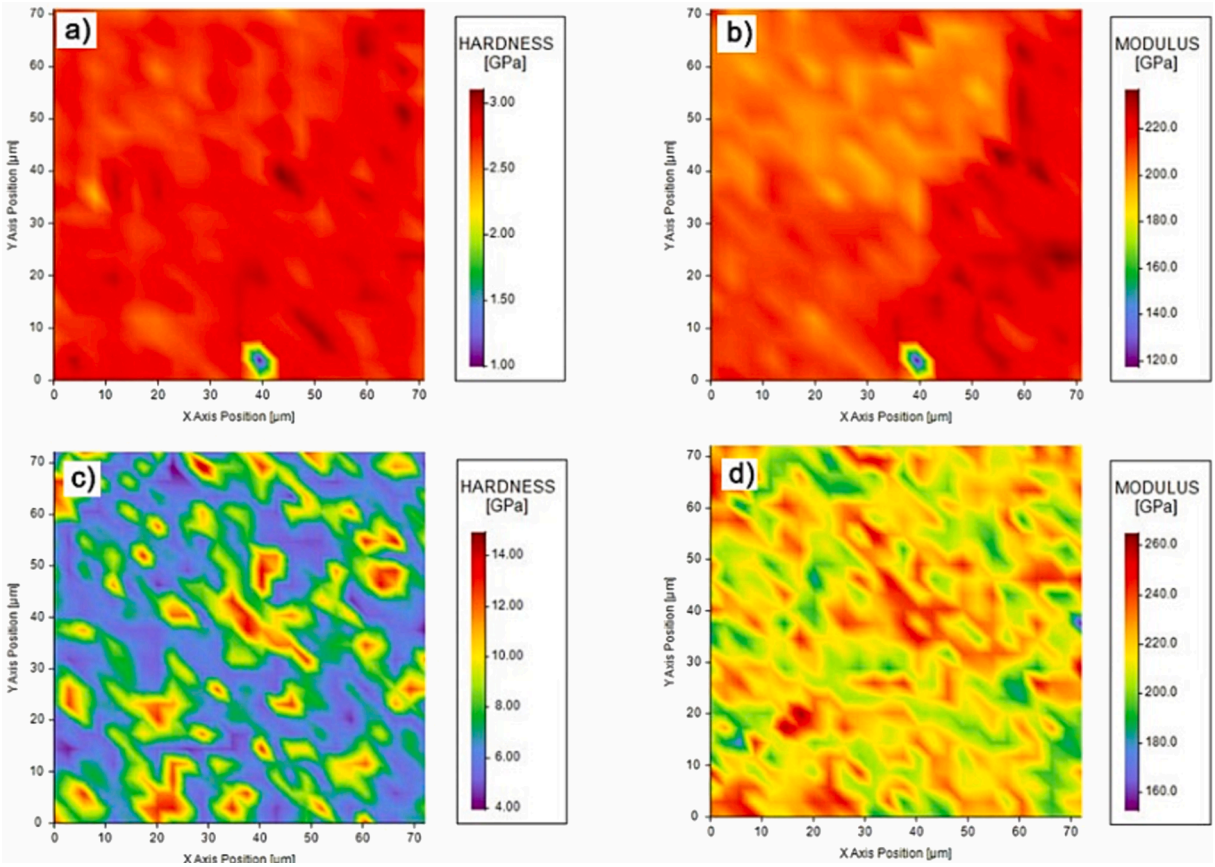

Fig. 5. Hardness and modulus maps for a), b) CoCrFeMnNi (Ti0), c) and d) $CoCrFeMnNiTi_{0.3}$ (Ti0.3) HEAs.

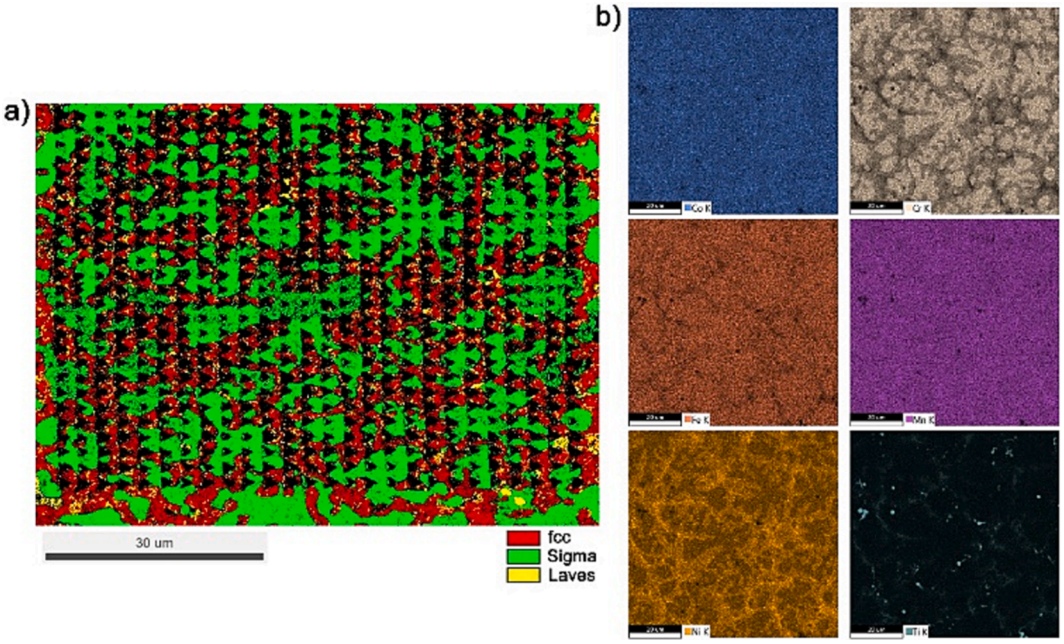

Fig. 6. (a) EBSD phase map and (b) chemical distribution across the indentation field of the $CoCrFeMnNiTi_{0.3}$ (Ti0.3) alloy.

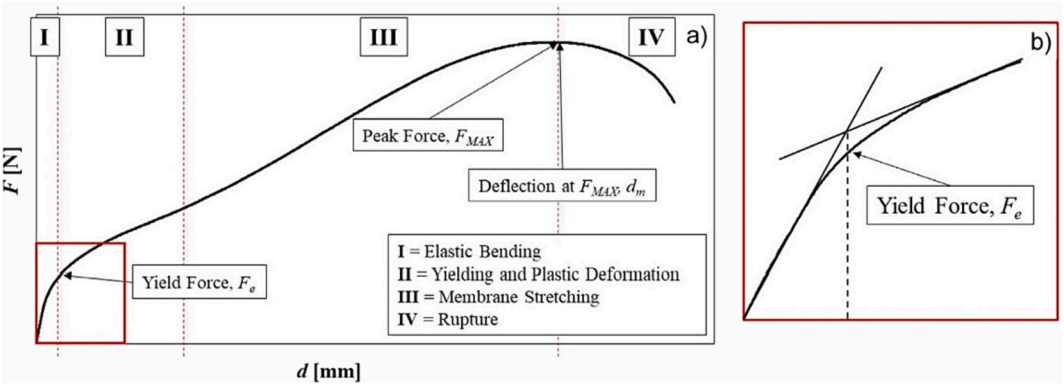

Fig. 7. (a) Example shear punch shear stress–deflection curve with different deformation zones indicated, (b) Determination of τ_{PS} [11].

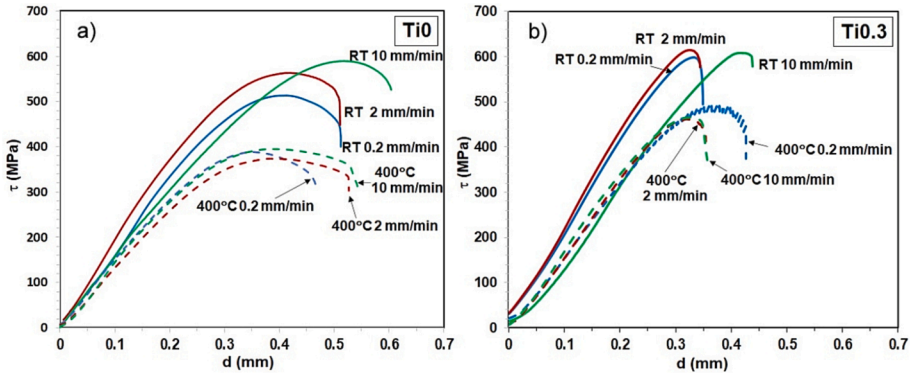

Fig. 8. Shear punch shear stress–deflection behaviour at RT and at 400 °C at deflection rates of 0.2, 2 and 10 mm•min^{-1} for a) CoCrFeMnNi (Ti0) and b) $CoCrFeMnNiTi0_{.3}$ (Ti0.3) HEA compositions.

nm indentation depth. The strain rate sensitivity exponent, *m,* was determined at the strain rate change at 1500 nm indentation depth.

3. Results and discussion

3.1. Microstructural characterization of as-cast alloys

The microstructures of the HEA alloys were captured with X-ray

Table 2
Ultimate shear stress values for CoCrFeMnNi (Ti0) and CoCrFeMnNi$Ti_{0.3}$ (Ti0.3) HEA compositions for different testing temperatures and strain rates.

Strain rate (mm•min^{-1})	CoCrFeMnNi		CoCrFeMnNiTi0.3	
	RT	400 °C	RT	400 °C
	τ_{USS} (MPa)	τ_{USS} (MPa)	τ_{USS} (MPa)	τ_{USS} (MPa)
0.2	513.70	388.03	597.79	491.32
2	562.99	374.86	614.52	462.08
10	590.68	395.39	608.82	465.71

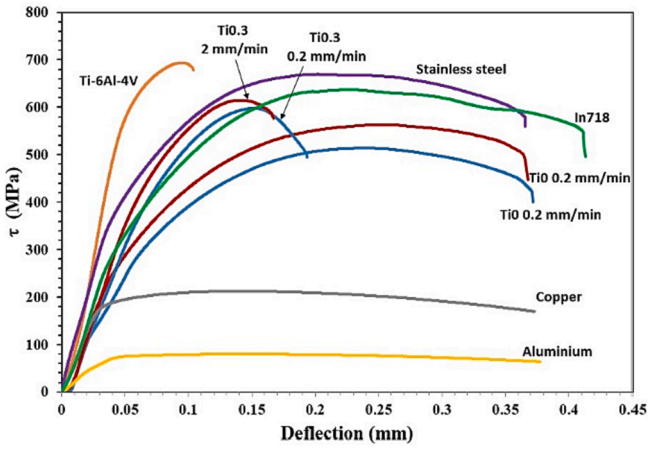

Fig. 9. ShP shear stress–deflection behaviour at RT for some commercially available alloys tested at 0.5 mm.min^{-1} and for Ti0 and Ti0.3 tested at 0.2 and 2 mm.min^{-1}.

diffraction (XRD), Scanning Electron Microscopy (SEM) and Transmission Electron Microscopy (TEM). The XRD peaks for CoCrFeMnNi (coded at Ti0) and CoCrFeMnNi$Ti_{0.3}$ (coded as Ti0.3) alloys are shown in Fig. 2 and show that the Ti0 alloy is attributed to a single FCC phase while for Ti0.3 there are peaks associated to the σ phase in addition to the FCC peaks. The Ti0 material consists of a single FCC structure with XRD peaks at 43.18° (111), 50.45° (200) and 74.16° (220) for which the d-spacings (in Å) of the different (*hkl*) planes are d(111) = 2.093, d(200) = 1.807 and d(220) = 1.278 Å, and therefore the lattice constant is 3.618 Å. However, for Ti0.3 the XRD peaks are attributed not only to FCC but also to a σ phase. The σ phase peaks match with the (202) and (331) peaks of those previously identified in the first report of its kind that has indexed the σ phase of HEAs [24]. The FCC peaks are detected at 43.18° (111), 50.42° (200) and 89.80° (311) for which the d-spacings (in Å) of the different (*hkl*) planes are d(111) = 2.093, d(200) = 1.809 and d(311) = 1.091 Å, from which the calculated lattice constant is 3.621 Å. The slightly larger lattice constant than 3.618 Å for Ti0 could be attributed to the additional presence of Ti in solid solution in the Ti-containing alloy. Both compositions were suction casted at the same cooling rate, $\dot{T}$, which can be estimated from the relationship [25]:

$$\dot{T}\left(\frac{K}{s}\right) = \frac{10}{R^2}\left(\frac{1}{cm^2}\right) \quad (2)$$

Where R (4 mm) is the sample radius, and therefore $\dot{T}$ is ~ 250 K/s.

To better understand the microstructural and compositional differences between the two HEAs, backscattered SEM images and compositional X-ray mappings (Fig. 3) were gathered. The Ti0 alloy has an almost featureless microstructure (Fig. 3a) although two regions with minor differences in chemical composition exist, thus suggesting the existence of chemical segregation with one region rich in Mn and Ni, and the other one rich in Fe, Co and Cr. For the Ti0.3 composition (Fig. 3b), the microstructure consists of distinct phases with dendrites of grey tonality, rich in Cr and Fe while the interdendritic region (clear tonality from backscattered SEM) is Ti-rich. The distribution of the elements Mn, Co and Ni seem evenly distributed within both phases. The dark spots for CoCrFeMnNi HEA (white arrows) are attributed to the presence of porosity, which are characterised by their round geometry. However, for Ti0.3, in addition to the porosity (as indicated by the white arrows), irregular dark areas (indicated by the black arrows) of the same tonality are present, which are very rich in Ti and poor in the other elements and therefore could be associated to segregation of Ti upon suction casting.

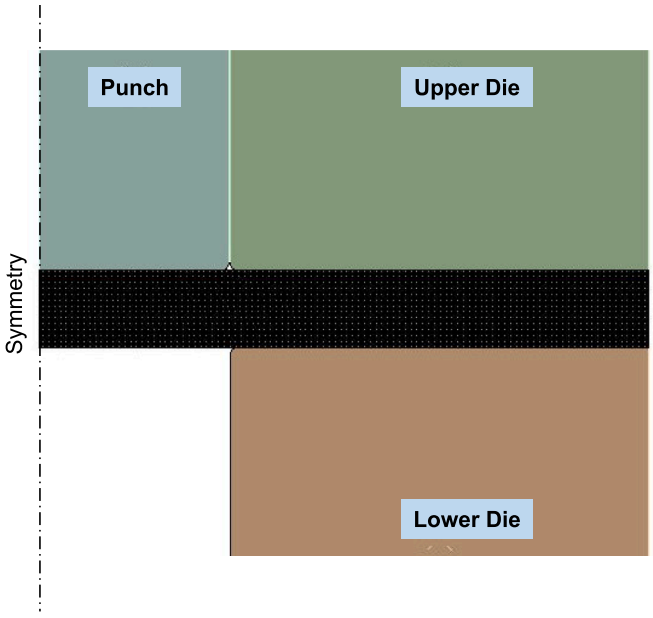

Fig. 10. Numerical model of the shear punch test.

Table 3
Predicted uniaxial properties for CoCrFeMnNi (Ti0) and CoCrFeMnNi$Ti_{0.3}$ (Ti0.3) HEA compositions derived from ShP tests.

	Deflection rate (mm•min^{-1})	Temp. (°C)	τ_{USS} (MPa)	τ_{PS} (MPa)	Predicted σ_{UTS} (MPa)	Predicted σ_y (MPa)
CoCrFeMnNi	0.2	20	514	268	704	432
CoCrFeMnNi	2	20	563	256	767	415
CoCrFeMnNi	10	20	591	200	801	338
CoCrFeMnNi	0.2	400	388	117	546	222
CoCrFeMnNi	2	400	375	115	530	219
CoCrFeMnNi	10	400	395	111	555	214
CoCrFeMnNi$Ti_{0.3}$	0.2	20	598	357	811	556
CoCrFeMnNi$Ti_{0.3}$	2	20	615	382	832	591
CoCrFeMnNi$Ti_{0.3}$	10	20	608	321	823	506
CoCrFeMnNi$Ti_{0.3}$	0.2	400	491	312	676	493
CoCrFeMnNi$Ti_{0.3}$	2	400	462	295	639	470
CoCrFeMnNi$Ti_{0.3}$	10	400	466	156	644	276

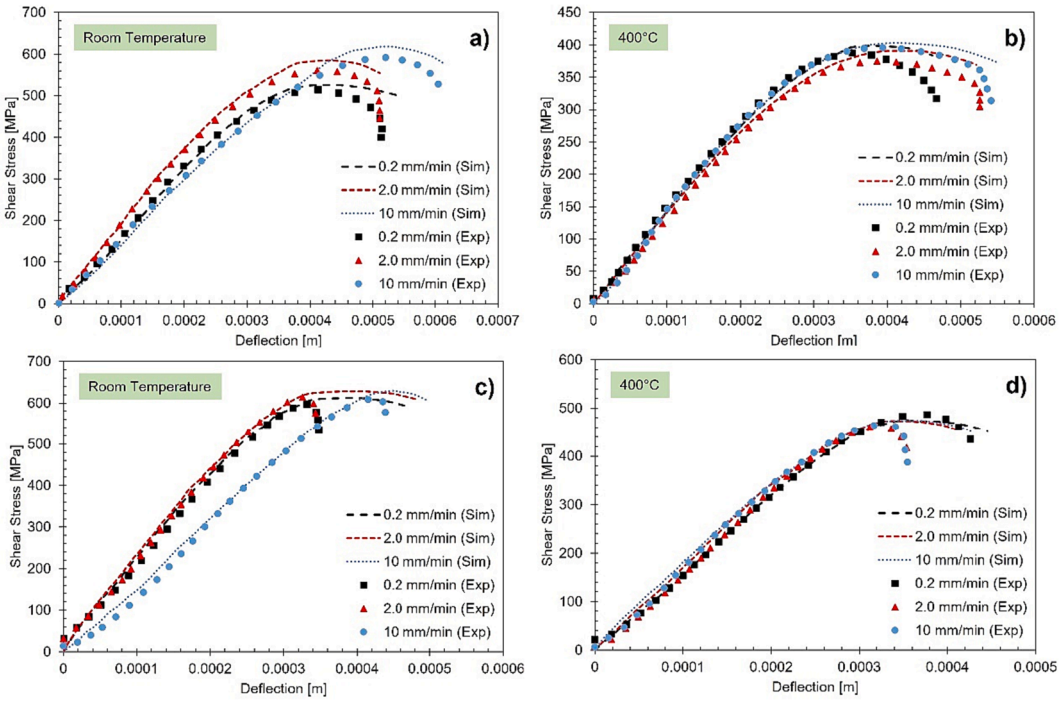

Fig. 11. Comparison of the shear stress–deflection curves between the experiments (exp) and simulations (sim) for different deflection rates for a) CoCrFeMnNi (Ti0), RT, b) CoCrFeMnNi (Ti0), 400 °C, c) CoCrFeMnNi$Ti_{0.3}$ (Ti0.3), RT and d) CoCrFeMnNi$Ti_{0.3}$ (Ti0.3), 400 °C.

To better understand the microstructural differences between the two compositions, additional SEM images were collected across two magnifications. Fig. 4 shows the backscattered SEM images for Ti0 (Fig. 4a and 4b) and Ti0.3 (Fig. 4c and 4d), measured from the central radius of the samples. For the Ti0.3 alloy, a microstructure consisting of 3 phases is observed, where the grey dendrites are very abundant and constitute the matrix (~63 % vol.) while the interdendritic phase consist of white regions (~27 % vol.) that encapsulate a grey phase (~2 % vol.). In addition, black areas (~8 % vol.) of irregular distribution and a size of up to 2 μm are observed. Some of them seem to have close to a round shape while others are more polygonal and therefore could be attributed to a mixture of porosity and to Ti segregated upon solidification. In fact, the dark tonality is consistent with the low atomic weight of Ti (47.867 g/mol) compared to that of the other elements, (Co (58.933 g/mol), Cr (51.996 g/mol), Fe (55.485 g/mol), Mn (54.938 g/mol) and Ni (58.693 g/mol)). Due to the similarity in tonality, their volume fraction have been counted together (~8 % vol.) as listed in Table 1. Similar microstructures have been previously reported by Qin et al. although they studied compositions with a higher concentration in Ti [26]. The white regions were found to be rich in Ti and Co (13.1 ± 0.5 and 18.9 ± 0.2 at. %, respectively) and such a composition corresponds to the σ phase. The encapsulated dark grey phase is rich in Ti, a low atomic weight element, which can explain their relatively dark tonality and would correspond to a Laves phase. The small volume fraction is close to the detection limit, which may explain the lack of XRD peaks associated to this phase (Fig. 2). This phase could correspond to a Co_2Ti type Laves phase, since according to previous observations, this phase has a similar concentration of Ti [27]). The volume fraction of the different crystalline phases (vol. %) are listed in Table 1.

3.2. Mechanical characterization

Prior to proceeding with the small and shear punch testing, a nano scale mechanical assessment was carried out to characterize the properties of the phases present in the two HEA compositions. For this reason, the indentation modulus and hardness of the different microstructural features of the Ti0 and Ti0.3 HEAs were studied by means of nanoindentation mapping. As given in Fig. 5a and b, the Ti0 alloy shows a homogenous distributed hardness and modulus in the range of 2.75 and 210 GPa, respectively. The hardness mapping of the Ti0.3 alloy clearly reveals strongly varying mechanical properties (H ≈ 8 – 12 GPa), indicating the presence of the different phases. The regions indicated by the blue colour (~4 GPa) may correspond to the soft FCC phase. Hardness values in the range of 14 GPa can be associated with the σ-phase and/or Laves phase. The green areas correspond to a compositional transition and therefore exhibits intermediate hardness. The high hardness (>14 GPa), could be expected taking into consideration that the σ and Laves phase are intermetallic compounds. The Young's modulus of the FCC matrix (as given by green coloured regions) is approximately 200 GPa, which is close to the average value of that for the Ti0 alloy, as derived previously both in this work and from published sources [27–29] and reaches 240–260 GPa for the σ phase and the Laves phase. Although a local correlation of the mechanical properties and the phases present at the surface can be performed (Fig. 5 and Fig. 6), it is not possible to identify the sub-surface phase distribution using EBSD. This means that a straightforward assignment of the hardness and modulus data to the phases determined by EBSD cannot be directly applied, as the mechanical properties are averaged over the plastic zone below the indent and thus several phases can be measured at the same time.

3.3. Strain rate sensitivity

The resistance to creep deformation is an important property to consider for any material envisaged to be used at an elevated service temperature. The tendency for a material to creep can be assessed by measuring the strain rate sensitivity, SRS (i.e., when SRS is close to zero, there is no creep present), which can be calculated from the equation [30]:

$$\sigma = K\dot{\varepsilon}^m \tag{3}$$

43280071016000Where σ is the flow stress and it is a function of K, a material constant, represents the strain rate and m the strain rate sensitivity factor. From Eq. (3), the strain rate sensitivity factor can be

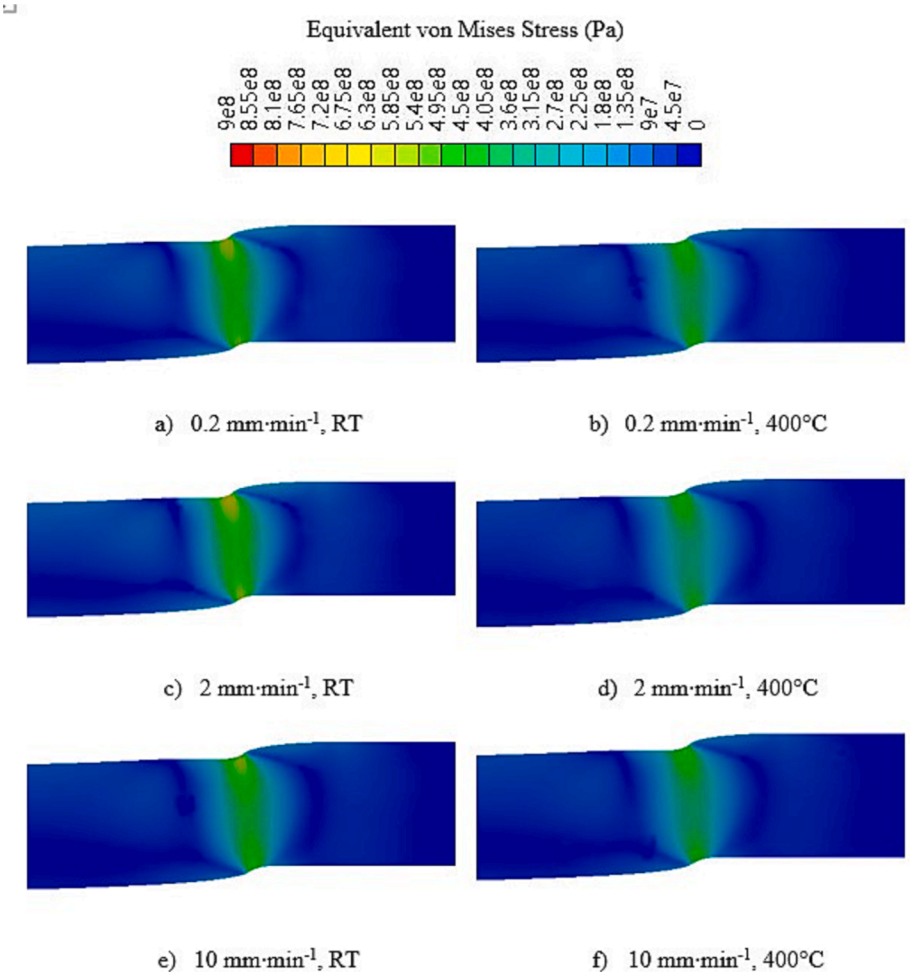

Fig. 12. Equivalent von Mises stress distribution for the CoCrFeMnNi (Ti0) HEA alloy at different deflection rates at room temperature and 400 °C.

obtained [31]:

$$m = \frac{d\ln\sigma}{d\ln\dot{\varepsilon}} \tag{4}$$

775188571500where σ and represent the flow stress and the strain rate, respectively. To determine the strain rate sensitivity using small specimen discs, the SP test can be employed, which was previously utilised by the authors to characterize the properties of ductile HEAs such as CoCrFeMnNi [18].

An alternative approach to assess the mechanical properties is shear punch (ShP) testing, where the force is applied via a flat ended punch, compressively forcing the material through a recess with a tight tolerance to induce shear in the material [11]. Since the ShP test results in a more uniform stress state throughout the sample when compared to SP, it would be expected that ShP tests would offer a more suitable means of obtaining the strain rate sensitivity of relatively brittle materials. Moreover, as previously found, the ShP test is more relatable to uniaxial tensile properties than SP generated results, given the nature of shear deformation that takes place under ShP loading [11].

Fig. 7 shows an example of a shear punch shear stress–deflection curve, which, similarly to uniaxial tensile tests, consists of 3 regions: Region I relates to a linear elastic region until a yield point is reached, which corresponds to shear yield stress (τ_y); Region II refers to a period of plastic deformation between τ_y and the ultimate shear stress (τ_{USS}) and Region III reflects the final stage of rupture, when failure occurs.

The results from the ShP tests on the HEA alloys are given in Fig. 8. For the room temperature tests on the Ti0 composition (Fig. 8a), τ_{USS} increases from 513.7 MPa at 0.2 mm•min^{-1} to 562.98 and 590.67 MPa when the strain rate increases from 2 to 10 mm•min^{-1}. However, when tested at 400 °C at the same strain rates, the τ_{USS} values are lower, ranging from 374 to 395 MPa, and do not follow a clear trend, thus suggesting the Ti0 alloy does not exhibit a strain rate sensitivity at 400 °C. For the Ti0.3 HEA (Fig. 8b), τ_{USS} values are higher than for Ti0 HEA at both RT and at 400 °C, which is consistent with the higher average hardness values generated from nanoindentation (Fig. 5). This could be expected since the hardness and the strength are correlated through the equation σ_{UTS} / Hv = 3.45 [32] where Hv is the Vickers hardness and σ_{UTS} is the ultimate tensile strength. For the Ti0.3 HEA alloy, the τ_{USS} values remain very similar at a given temperature despite the change in strain rate, indicating the Ti0.3 HEA does not exhibit a strain rate sensitivity for the strain range used. The τ_{USS} values for the two different alloys across the different deflection rates and temperatures are listed in Table 2.

To further understand the mechanical performance of these HEAs when subjected to ShP testing, the results have been compared with those for commercially available alloys tested at RT at 0.5 mm•min^{-1} (i.e., intermediate between 0.2 and 2 mm•min^{-1}) as shown in Fig. 9. While for copper and aluminium the τ_{USS} values are lower than 250 MPa, for In718, stainless steel and Ti-6Al-4 V the value of τ_{USS} ranges from 600 to 700 MPa. Therefore, the hardest alloy, the Ti0.3 HEA, exhibits τ_{USS} values similar to those of stainless steel (~670 MPa) and Inconel 718 (~640 MPa). The ductility for Ti0.3 HEA is also similar to that of stainless steel and is more ductile than Ti-6Al-4 V.

In previous research, Lancaster et al. [11] correlated the shear punch results to uniaxial tensile data. In order to derive the shear offset proof stress (τ_{PS}), the τ - d/t curve was intercepted by a shear stress offset line

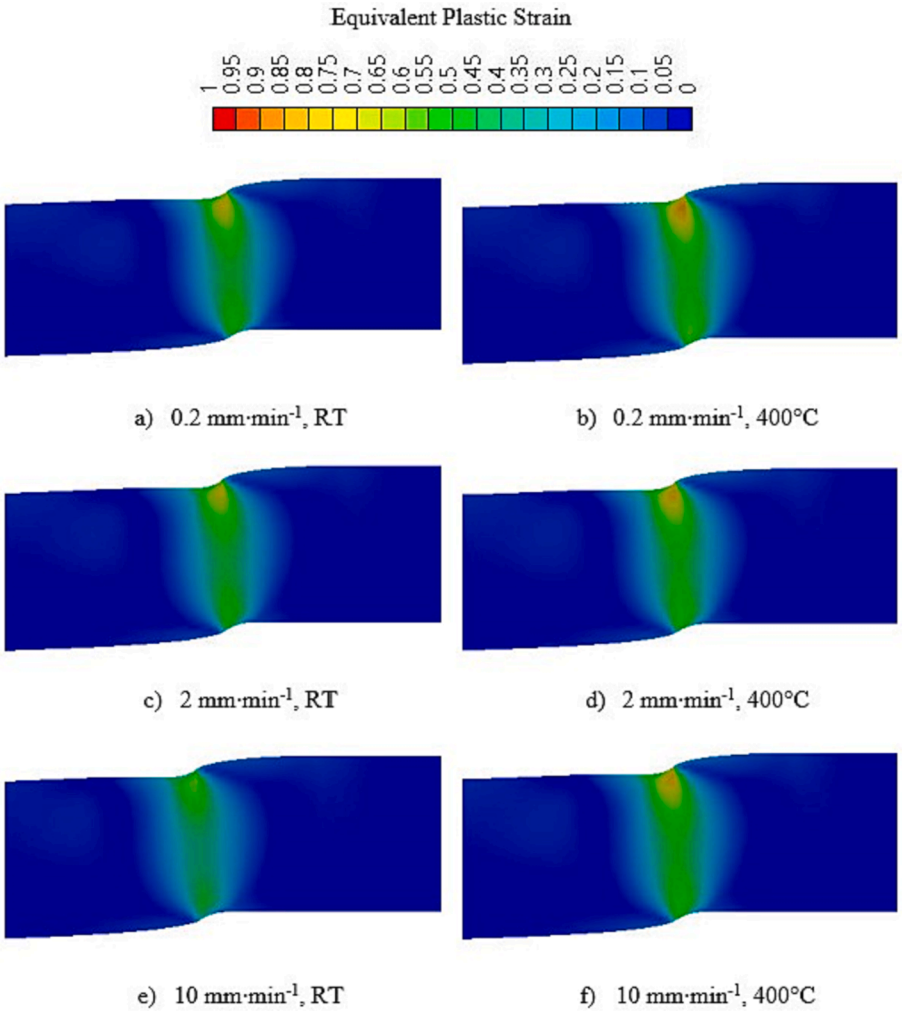

Fig. 13. Equivalent plastic strain distribution for the CoCrFeMnNi (Ti0) HEA alloy at different deflection rates at room temperature and 400 °C.

parallel to the linear section (Fig. 7b), as also previously reported by Kobayashi et al. [33], where d is the deflection and t the sample disc thickness. From here, the authors derived τ_{PS} and τ_{USS} from ShP experiments to correlate to tensile yield strength (σ_y) and ultimate tensile strength (σ_{UTS}) from the following equations:

$$\sigma_{PS} = m_1 \tau_{PS} + n_1 \tag{5}$$

$$\sigma_{UTS} = m_2 \tau_{USS} + n_2 \tag{6}$$

where $m_{1,2}$ and $n_{1,2}$ are constants. Lancaster et al. [11] derived these values to be $m_1 = 1.3909$, $m_2 = 1.261$, $n_1 = 59.403$, $n_2 = 56.668$, from a series of ShP tests on the materials depicted in Fig. 9, namely aluminium, copper, stainless steel, Inconel 718 and Ti-6Al-4 V. Based on these constants, predicted uniaxial properties for the two HEA compositions could be calculated, as given in Table 3.

In order to assess the experimental results and the efficacy of the empirical predictions, simulations of the ShP test results have been conducted for the different deflection rates.

3.4. Finite element simulation

3.4.1. Numerical model

Finite Element (FE) simulations of the deformation behaviour of the two HEA compositions under ShP loading were performed to analyse the stress and strain distributions under different strain rates, which cannot be obtained from the experiments. The FE simulations were conducted using a commercial structure code ANSYS Mechanical 2022R1. In order to be computationally efficient, a two-dimensional (2D) axisymmetric model, centred about the axis of the punch, was used to carry out the simulations. The numerical model employed in this study is shown Fig. 10. In this model, the punch, the upper die and the lower dies are treated as rigid bodes, whereas the specimen is specified to be flexible. The specimen body is meshed using the ANSYS meshing. An 8-node quadrilateral element is utilised to generate the mesh. The mesh sensitivity study is also carried out, and it is found that a uniform element size of 0.01 mm over the entire specimen is sufficient to obtain the accurate results. The selected mesh contains 300,000 elements and it is depicted in Fig. 10.

3.4.2. Boundary conditions and numerical settings

A translational boundary condition was specified on the punch body with deflection rates consistent with the experiments (i.e., 0.2, 2 and 10 mm•min^{-1}) employed in the Y-direction as shown in Fig. 10. A part of the specimen body was vigorously positioned between the upper and lower dies to constrain the movement in the Y-direction. A frictional contact with a coefficient of 0.2 was specified between the specimen and the punch, and the specimen and the dies while the dies were fixed in all directions. The nonlinear behaviour of the material was considered by activating large deformation in the FEA simulation, and the solution was solved using the Newton-Raphson method. An automatic time-stepping method was activated to ensure that the time-step used in every iteration was small enough for the deformation of the specimen based on the

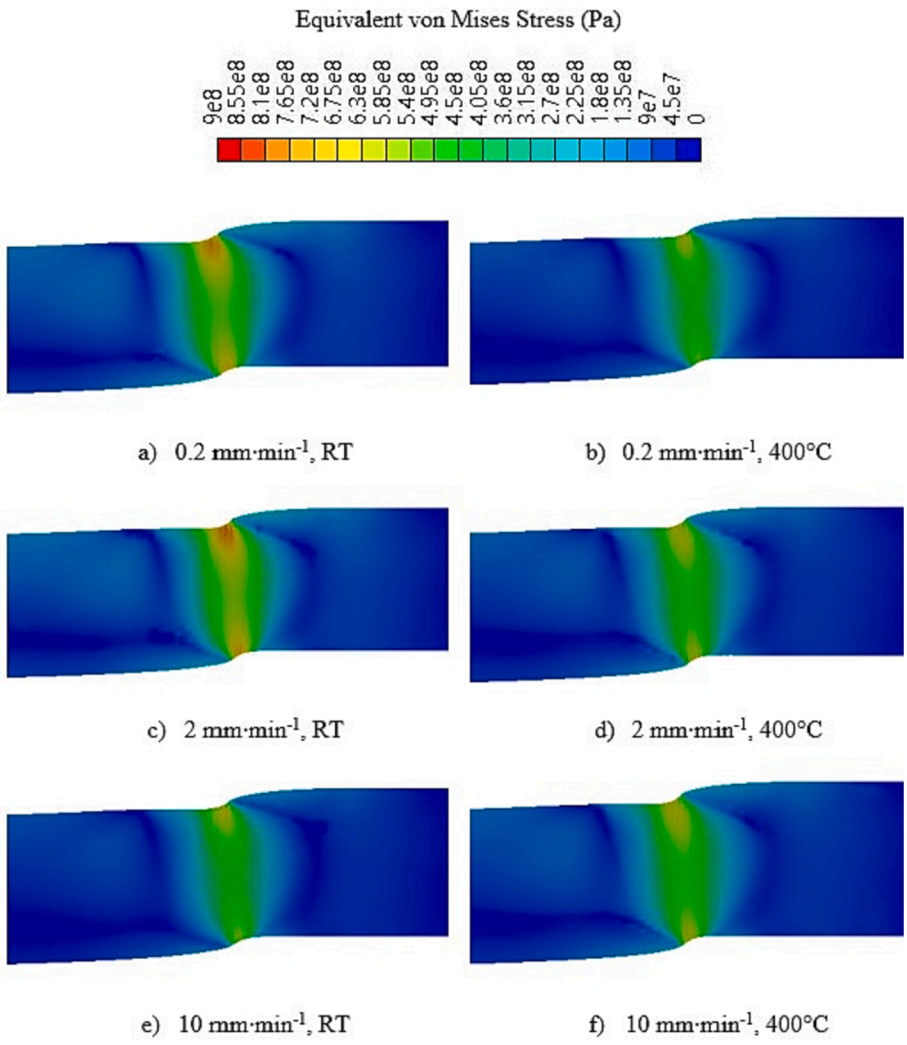

Fig. 14. Equivalent von Mises stress distribution for the $CoCrFeMnNiTi_{0.3}$ (Ti0.3) HEA alloy at different deflection rates at room temperature and 400 °C.

applied deflection rate.

3.4.3. *Material properties*

Nonlinear materials were created in the Engineering Data section in ANSYS for each of the two HEA compositions. An isotropic model was used to define the linear elastic properties of the material, and a multilinear isotropic hardening model was employed to define the plasticity and nonlinear characteristics of the material. In this paper, the Johnson-Cook model was used to construct the stress–strain relationship for the material properties. The stress–strain relationship based on the hardening of the material could be fitted using the following equation.

$$\sigma = \sigma_y + k\epsilon^n \tag{7}$$

In the above equation, σ_y, k and n are the yield strength, the strength coefficient, and the strain hardening exponent, respectively. At a reference strain rate, the Johnson-Cook equation could be expressed as:

$$\sigma = A + B\epsilon^n \tag{8}$$

where, A, B and n parameters are related to σ_y, k and n in Equation (7), and these parameters are estimated from the experimental data. The equations to correlate σ_y, σ_{UTS} and the relevant shear stress equivalents measured from the experiments are given in Equations (5) and (6), and they are used to estimate A and B parameters, while the hardening exponent n is varied for the fitting. Equation (1) can be used to compute the shear stress (τ) from the load- deflection curve obtained from the FEA simulations.

The shear stress- deflection curves generated from the ShP experiments (exp.) on the two HEA compositions at RT and 400 °C are compared to those produced in the FEA simulations (sim.) in Fig. 11. The experimental and simulated curves show good agreement with one another, up until where the τ_{USS} point I is reached and the specimen starts to rupture. This is due to the absence of a damage model in the simulations. Despite this, the results indicate that the first and the second zones of the curves obtained from the simulations fit well with those of the experiments, and it is, therefore, noted that the simulated results are reliable enough for further analyses. There is a period of plastic instability in the rupture region beyond the maximum stress where the fitting is not as effective, however, this is consistent with previous reports which employ the FEA models for small punch tests or shear punch tests [11,18].

Performing FEA simulations enables both qualitatively and quantitatively analyses of the stress and strain distributions across the miniature disc specimen when subjected to different strain rates, which cannot be obtained from the experiments itself. The von Mises stress distributions across Ti0 HEA disc samples under the different strain rates and temperatures are compared in Fig. 12. The stresses are extracted at a fixed deflection value of 0.3 mm, which lies between the yield and maximum stress values. It is seen that the stresses are originated within the shear zone of the specimen due to the external force applied by the punch, which then redistribute into a wider region in the radial

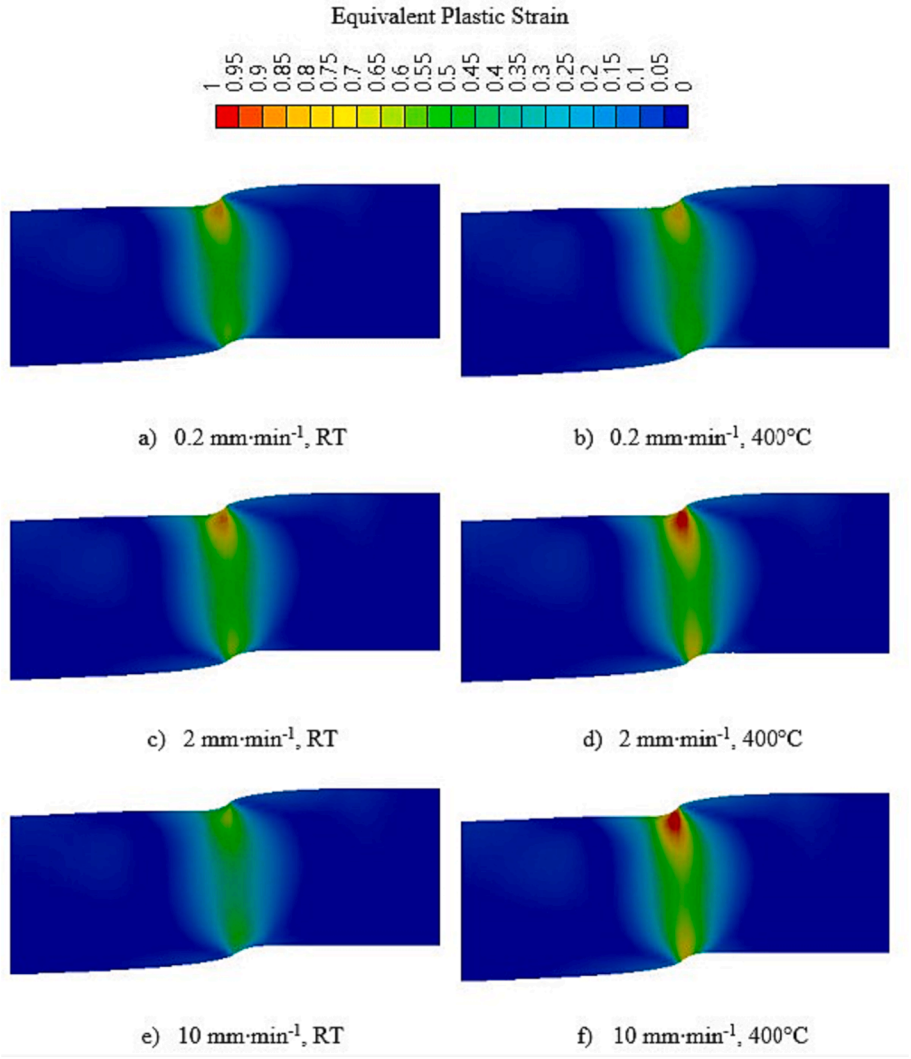

Fig. 15. Equivalent plastic strain distribution for the $CoCrFeMnNiTi_{0.3}$ (Ti0.3) HEA alloy at different deflection rates at room temperature and 400 °C.

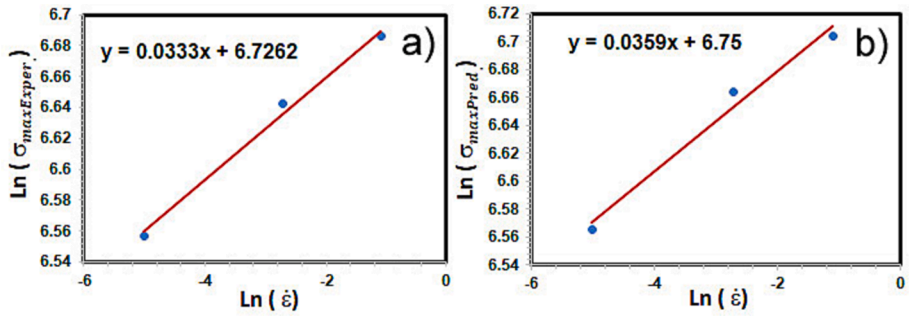

Fig. 16. Plot Ln max. stress-Ln strain rate for the a) experimental and b) simulated stresses for CoCrFeMnNi HEA tested at RT.

direction. At a deflection rate of 2 mm.min^{-1}, the highest concentration in stress is observed within the shear zone, which is consistent with the stress value presented in Table 3. Raising the temperature to 400 °C decreases the distribution within the specimen, and the variation of stresses at different strain rates are also in excellent agreement with Table 3. The equivalent plastic strain variations at a fixed deflection of 0.3 mm are illustrated in Fig. 13. The plastic strains are initiated within the shear zone as the force is applied by the punch. A similar strain distribution is detected between different deflection rates at both room temperature and 400 °C. Although, the strains are higher at 400 °C as it is closer to the maximum stress compared that at room temperature.

The contours of the equivalent von Mises stress and plastic strain for the Ti0.3 HEA composition under different deflection rates at room temperature and 400 °C are depicted in Figs. 14 and 15. As was the case for the simulations for the Ti0 HEA alloy, the contours are extracted at a fixed deflection of 0.3 mm. The stress distribution at the deflection rate of 2 mm•min^{-1} at room temperature is noticeably higher than the rest of the simulations, which is in a good agreement with the values given in Fig. 11 and Table 3. It is observed that the stresses at 400 °C are significantly lower than that of the room temperature. The plastic strain

Table 4
Comparison of the maximum stress values for the different strain rates obtained through empirical equations from the shear punch data and FEA simulations.

	Deflection rate (mm•min^{-1})	Temp. (°C)	Maximum Stress (MPa), Experiment	Maximum Stress (MPa), Simulation
CoCrFeMnNi	0.2	20	704	710.37
CoCrFeMnNi	2	20	767	783.72
CoCrFeMnNi	10	20	801	815.74
CoCrFeMnNi	0.2	400	546	559.44
CoCrFeMnNi	2	400	530	539.33
CoCrFeMnNi	10	400	555	564.67
CoCrFeMnNiTi$_{0.3}$	0.2	20	811	829.03
CoCrFeMnNiTi$_{0.3}$	2	20	832	850.48
CoCrFeMnNiTi$_{0.3}$	10	20	823	848.62
CoCrFeMnNiTi$_{0.3}$	0.2	400	676	666.29
CoCrFeMnNiTi$_{0.3}$	2	400	639	652.82
CoCrFeMnNiTi$_{0.3}$	10	400	644	654.34

distributions of the Ti0.3 composition is clearly higher than that of Ti0, as the deflection of 0.3 mm is close to the maximum stress (see Fig. 11) except in the simulations of 10 mm•min^{-1} at room temperature and 0.2 mm•min^{-1} at 400 °C.

In order to calculate the strain rate sensitivity of Ti0 at RT, the only alloy and condition for which a clear trend for the maximum stress versus strain is observed, the Ln of the strain rate versus the Ln of the maximum stress have been plotted (Fig. 16).

The values listed in Table 4 have been used for the plots of Fig. 16. The SRS value for the experimental results is $m = 0.0333$, while for the predicted correlation it is $m = 0.0359$ and therefore the difference is very small, thus suggesting excellent agreement with the FEA simulation. The difference between the experimental and predicted values for CoCrFeMnNi are smaller than that previously seen using SP testing, where the m values were 0.1387 and 0.1313, respectively [18], thus indicating a higher level of reliability. The values derived here are one order of magnitude smaller than those from SP testing at room temperature, thus indicating the Ti0 HEA is less sensitive to the ShP loading conditions. Moreover, at 400 °C the Ti0 HEA is strain rate insensitive and therefore resistant to creep, at least for the shear stress conditions applied here. This implies, therefore, that the alloy could have important technological applications, for example in rivets and bolts for aircrafts since they are generally subjected to high shear stress conditions. The experimental value, m = 0.0333, is close to 0.028 obtained for quasi-static compression tests at similar strain rates, from 0.024 mm.min^{-1} to 2.4 mm.min^{-1} [34] while Shabani et al. obtained for uniaxial tensile experiments m = 0.048 for CoCrFeMnNi (Cantor) and m = 0.044 for CoCrFeNi [35]. These values are smaller than m ~ 0.5 for FCC metals such as Cu, Ni and Au when tested in tension at very slow strain rates since diffusional mechanisms such as grain boundary sliding start to be important at very slow strain rates [36]. For CoCrFeMnNi, the m value is smaller may be due to the enhanced contribution of solid solution strengthening [37] and resultant sluggish diffusion while for Ti$_{0.3}$ the strain rate insensitivity is probably associated to the enhanced solid solution as demonstrated before from the lattice constant increase from 3.618 Å for Ti0 to 3.621 Å for Ti0.3. To the author's knowledge this is the first time that ShP has been used to determine the SRS of Ti0 and Ti0.3 HEAs.

On the other hand, the Ti0.3 HEA composition exhibits higher strength than the Ti0 material but it is insensitive to the strain rate, both at room temperature and at 400 °C. Therefore the Ti0.3 composition could be useful as a structural material to support high shear stresses, including rivets and bolts, but not for fail-safe mechanisms or components that absorb kinetic energy due to the more brittle nature of the composition.

3.4.4. *Nanoindentation strain rate jump testing*

Nanoindentation strain rate jump tests were performed to investigate the strain rate sensitivity on a local scale according to [19]. The tests were performed to a maximum indentation of 2500 nm in order to reduce the influence of the indentation size effect (ISE) in these coarse-grained materials (Fig. 17) [20]. While the single phase Ti0 HEA alloy shows very little scatter in the hardness (Hv) – indentation depth plot (Fig. 17a), the multiple phases present in the Ti0.3 HEA alloy exhibit a large degree of scatter in the indentation SRJ data (Fig. 17b). Although it is a common procedure to determine the strain rate sensitivity exponent m through $m = \frac{d(lnH)}{d(ln\dot{\varepsilon})}$), it should be noted that multiple phases may be present in the plastic zone beneath the indenter with changing volume fractions and ratios due to the multiphase microstructure. Furthermore, it should be noted that the microstructure beneath the indenter may be unstable during indentation [21]. Hence, the change in hardness with changing strain rate can be used to determine the SRS of the Ti0 alloy, but this procedure is not feasible for the multiphase Ti0.3 alloy due to the amount of scatter that arises, resulting in meaningless values of m. The present study reveals a strain rate sensitivity exponent m of 0.009 ± 0.001 for the Ti0 HEA alloy, which is in good agreement with various literature [22,23].

4. Conclusions

The research presented in this paper has examined the suitability of using the small and shear punch test methods in understanding the SRS of two high-entropy alloy (HEA) CoCrFeMnNiTi$_x$ compositions at both room temperature and 400 °C. From this work, the following conclusions can be drawn:

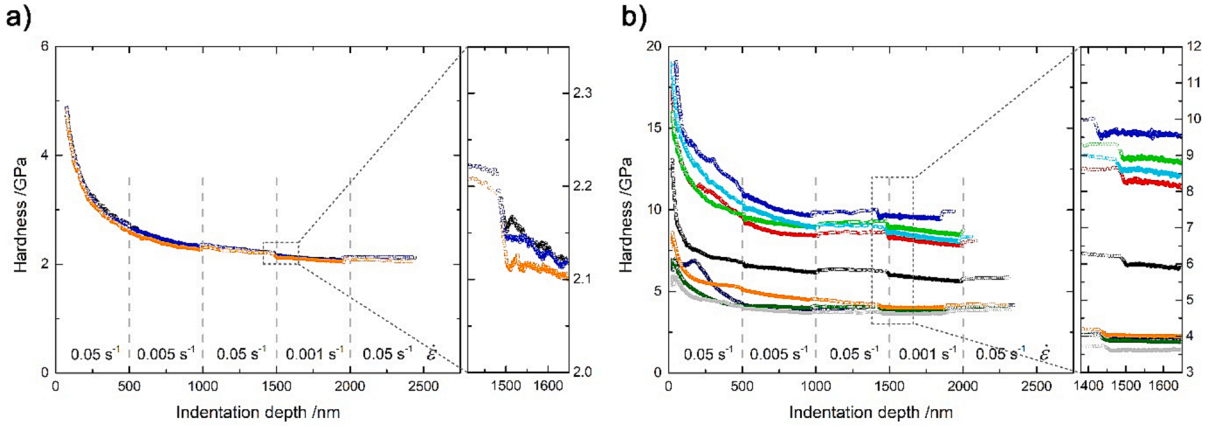

Fig. 17. Nanoindentation strain rate jump tests on a) equiatomic CoCrFeMnNi (Ti0) and b) CoCrFeMnNiTi$_{0.3}$ (Ti0.3) HEA alloys.

- The two HEA compositions (Ti0 and Ti0.3) were produced by suction casting into 8 mm diameter cylinders. The Ti0.3 variant was found to contain both sigma and Laves phase, leading to an increase in strength but also a reduction in ductility.
- Nanoindentation findings confirms the existence of homogenously distributed hardness (~2.75 GPa) and modulus (~210 GPa) in the Ti0 composition, while the trials on the Ti0.3 variant confirms the presence of the brittle σ-phase and/or Laves phase (H ~ 14 GPa) embedded in a soft FCC phase (~4 GPa).
- Shear punch testing was revealed to be a more appropriate test methodology as the specimen deforms under pure shear, and has previously been found to correlate with uniaxial properties more effectively.
- FEA simulations show good agreement with the shear punch generated force–deflection curves, up until the point of maximum stress, after which the simulation diverges due to the absence of a damage component in the FEA model.
- Maximum stresses generated from the FEA simulations show excellent agreement with empirically derived uniaxial maximum stress predictions derived from the shear punch experimental data.
- From the strain rate sensitivity evaluation using the shear punch results on the two HEA compositions across different deflection rates and temperatures, only the Ti0 variant was found to exhibit a strain rate sensitivity at room temperature, albeit to a very small extent ($m = 0.0333$). This value is close to 0.028 for quasi-static compression tests and m = 0.048 for uniaxial tensile experiments.

CRediT authorship contribution statement

S. González: Conceptualization, Investigation, Writing – original draft, Writing – review & editing. **A.K. Sfikas:** Data curation. **S. Kamnis:** Data curation. **S.E. John:** Visualization, Investigation. **N.C. Barnard:** Visualization, Investigation. **C. Gammer:** Investigation. **J. Eckert:** Visualization, Investigation. **C.G. Garay-Reyes:** Investigation. **R. Martínez-Sánchez:** Investigation. **S.W. Naung:** Software, Validation. **M. Rahmati:** Software, Validation. **T. Keil:** Data curation. **K. Durst:** Investigation. **R.J. Lancaster:** Writing – review & editing.

Declaration of Competing Interest

The authors declare the following financial interests/personal relationships which may be considered as potential competing interests: Spyros Kamnis reports financial support was provided by UK Research and Innovation. Sergio Gonzalez Sanchez reports equipment, drugs, or supplies and travel were provided by Northumbria University. K. Dust reports equipment, drugs, or supplies was provided by German Research Foundation (DFG). Spyros Kamnis reports a relationship with Castolin Eutectic Ltd that includes: employment. NA has patent NA pending to NA.

Data availability

Data will be made available on request.

Acknowledgements

The authors would like to acknowledge the support from the UK Research & Innovation (UKRI-IUK) national funding agency. Project Grant: 53662 'Design of High-Entropy Superalloys Using a Hybrid Experimental-Based Machine Learning Approach: Steel Sector Application'. K.D. gratefully acknowledge the funding by the German Research Foundation (DFG) within the priority programme SPP2006 under Grant No. DU424/13–2.

References

[1] J.W. Yeh, S.K. Chen, S.J. Lin, J.Y. Gan, T.S. Chin, T.T. Shun, C.H. Tsau, S.Y. Chang, Adv. Eng. Mater. 6 (2004) 299.
[2] B. Cantor, I.T.H. Chang, P. Knight, A.J.B. Vincent, Mater. Sci. Eng. A 375–377 (2004) 213.
[3] J.W. Yeh, Ann. De. Chim. Sci. De. Mater. 31 (2006) 633.
[4] E.P. George, D. Raabe, R.O. Ritchie, Nat. Rev. Mater. 4 (2019) 515.
[5] H. Shahmir, M. Nili-Ahmadabadi, A. Shafiee, M. Andrzejczuk, M. Lewandowska, T. G. Langdon, Mater. Sci. Eng. A 725 (2018) 196.
[6] M.S. Mehranpour, H. Shahmir, A. Derakhshandeh, M. Nili-Ahmadabadi, J. Alloy. Compd. 888 (2021), 161530.
[7] H. Shahmir, M.L. Ahmadabadi, A. Shafiee, M. Andrzejczuk, M. Lewandowska, T. G. Landgon, Mater. Sci. Eng. A 725 (2018) 196.
[8] H. Shahmir, A. Dherakhshandeh, B. Hallsted, M.N. Ahmadabadi, Mater. Werkst. 52 (2021) 441.
[9] T.T. Shun, L.Y. Chang, M.H. Shiu, Mater. Sci. Eng. A 556 (2012) 170.
[10] T.J. Gordon, J. Mater. Sci. 56 (2021) 10707.
[11] R.J. Lancaster, S.P. Jeffs, B.J. Haigh, N.C. Barnard, Mater. Des. 215 (2022), 110473.
[12] P. Sellamuthu, P.K. Collins, P.D. Hodgson, N. Stanford, Mater. Des. 47 (2013) 258.
[13] R.K. Guduru, K.A. Darling, R. Kishore, R.O. Scattergood, C.C. Koch, K.L. Murty, Mater. Sci. Eng. A 395 (2005) 307.
[14] R. Khorshidi, A. Honarbakhsh-Raouf, R. Mahmudi, J. Alloy. Compd. 700 (2017) 18.
[15] F. Sun, B. Wang, F. Luo, Y.Q. Yan, H.B. Ke, J. Ma, J. Shen, Mater. Des. 190 (2020), 108595.
[16] W. Qiao, H.Y. Ye, H.J. Yang, W. Liang, B.S. Xu, P.K. Liaw, M.W. Chen, Intermetallics 36 (2013) 31.
[17] K. Wang, Z. Ning, M. Li, J. Sun, Y. Huang, J. Alloy. Compd. 887 (2021), 161415.
[18] S. González, A.K. Sfikas, S. Kamnis, S.E. John, Z.W. Nye, M. Spink, C. Allen, R. Martínez-Sánchez, S.W. Naung, M. Rahmati, T. Keil, K. Durst, R.J. Lancaster, J. Alloy. Compd. 936 (2023), 168219.
[19] V. Maier, K. Durst, J. Mueller, B. Backes, H.W. Höppel, M. Göken, J. Mater. Res. 26 (2011) 1421.
[20] W. Nix, H. Gao, J. Mech. Phys. Solids 46 (1998) 411.
[21] T. Keil, E. Bruder, M. Laurent-Brocq, K. Durst, Scr. Mater. 192 (2021) 43.
[22] G.L. Hankin, M. Toloczko, K.I. Johnson, M.A. Khaleel, M.L. Hamilton, F.A. Garner, R. Davies, R.G. Faulkner, An Investigation into the Origin and Nature of the Slope and x-axis Intercept of the Shear Punch-Tensile Yield Strength Correlation using Finite Element Analysis, in: M.L. Hamilton, A.S. Kumar, S.T. Rosinski, M. L. Grossbeck (Eds.), Effects of Radiation on Materials: 19th International Symposium, ASTM International, West Conshohocken, PA, 2000, pp. 1018–1028.
[23] W.C. Oliver, G.M. Pharr, J. Mater. Res. 7 (1992) 1564.
[24] A.K. Sfikas, S. Kamnis, M.C.H. Tse, K.A. Christofidou, S. González, A.E. Karantzalis, E. Georgatis, Coatings 13 (2023) 1004.
[25] X. Lin, W. Johnson, J. Appl. Phys. 78 (1995) 6514.
[26] G. Qin, Z. Li, R. Chen, H. Zheng, C. Fan, L. Wang, Y. Su, H. Ding, J. Guo, H. Fu, J. Mater. Res. 34 (2019) 1011.
[27] L. Jiang, Y. Lu, Y. Dong, T. Wang, Z. Cao, T. Li, Intermetallics 44 (2014) 37.
[28] P. Lohmuller, L. Peltier, A. Hazotte, J. Zollinger, P. Laheurte, E. Fleury, Materials 11 (2018) 1337.
[29] H. Ge, H. Song, J. Shen, F. Tian, Mat. Chem. Phys. 210 (2018) 320.
[30] .L. Boyce, T.B. Crenshaw, M.F. Dilmore, The Strain-Rate Sensitivity of High-Strength High-Toughness Steels, Sandia Report, Sandia National Laboratories Albuquerque, New Mexico (2007).
[31] R.W. Hertzberg, Deformation and fracture mechanics of Engineering Materials, 4th Edition, John Wiley & Sons Inc, Hoboken, 1996.
[32] F. Khodabakhshi, M. Haghshenas, H. Eskandari, B. Koohbor, Mater. Sci. Eng. A 636 (2015) 331.
[33] T. Kobayashi, Y. Miura, M. Yamamoto, Tensile property evaluation of a Japanese reactor pressure vessel steel by Shear punch test technique. in: Proceedings of 5th International Small Sample Test Techniques Conference, 2018.
[34] J.M. Park, J. Moon, J.W. Bae, M.J. Jang, J. Park, S. Lee, H.S. Kim, Mater. Sci. Eng. A 719 (2018) 155.
[35] M. Shabani, J. Indeck, K. Hazeli, P.D. Jablonski, G.J. Pataky, J. Mater. Eng. and Perform 28 (2019) 4348.
[36] Q. Wei, S. Cheng, K.T. Ramesh, E. Ma, Mater. Sci. Eng. A 381 (2004) 71.
[37] R.B. Figueiredo, W. Wolf, T.G. Langdon, J. Mater. Res. Technol. 20 (2022) 2358.